

# Nucleon Polarizabilities: Theory

B. Pasquini<sup>1,a</sup>, D. Drechsel<sup>2,b</sup>, and M. Vanderhaeghen<sup>2,c</sup>

<sup>1</sup> Dipartimento di Fisica Nucleare e Teorica, Università degli Studi di Pavia,  
and INFN, Sezione di Pavia, I-27100 Pavia, Italy

<sup>2</sup> Institut für Kernphysik, Johannes Gutenberg-Universität, D-55099 Mainz, Germany

**Abstract.** We review recent developments in the theoretical investigation of the nucleon polarizabilities. We first report on the static polarizabilities as measured in real Compton scattering, comparing and interpreting the results from various theoretical approaches. In a second step, we extend the discussion to the generalized polarizabilities which can be accessed in virtual Compton scattering, showing how the information encoded in these quantities can provide a spatial interpretation of the induced polarization densities in the nucleon.

## 1 Introduction

The polarizabilities of a composite system such as the nucleon are elementary structure constants, just as its size and shape. They can be accessed experimentally by Compton scattering processes. In the case of real Compton scattering (RCS), the incoming real photon deforms the nucleon, and by measuring the energy and angular distributions of the outgoing photon one can determine the induced current and magnetization densities. The global strength of these densities is characterized by the nucleon dipole and higher order (quasi-static) polarizabilities. In contrast, the virtual Compton scattering (VCS) process is obtained if the incident real photon is replaced by a virtual photon. This virtuality of the photon gives access to the generalized polarizabilities (GPs) and allows us to map out the spatial distribution of the polarization densities.

Over the past years, the nucleon polarizabilities have been the subject of extensive experimental and theoretical studies (see, e.g., Refs. [1,2,3,4] for comprehensive reviews). In this work we summarize recent developments of the theoretical studies, and we refer to [5] for the corresponding analysis of the experimental work. In Sec. 2 we discuss the static polarizabilities and compare the predictions from different theoretical investigations. Several approaches to extract the polarizabilities from RCS data are presented in Sec. 3. The VCS process and the role of the GPs are reviewed in Sec. 4, and in Sec. 5 we discuss how to obtain a spatial representation of the information contained in the GPs. A short summary and some conclusions are given in Sec. 6.

---

<sup>a</sup> e-mail: [pasquini@pv.infn.it](mailto:pasquini@pv.infn.it)

<sup>b</sup> e-mail: [drechsel@kph.uni-mainz.de](mailto:drechsel@kph.uni-mainz.de)

<sup>c</sup> e-mail: [marcvdh@kph.uni-mainz.de](mailto:marcvdh@kph.uni-mainz.de)

## 2 Polarizabilities in RCS

The physical content of the nucleon polarizabilities can be visualized best by effective multipole interactions for the coupling of the electric ( $\mathbf{E}$ ) and magnetic ( $\mathbf{H}$ ) fields of a photon with the internal structure of the nucleon. When expanding the RCS amplitude in the energy of the photon, the zeroth and first order terms follow from a low-energy theorem and can be expressed solely in terms of the charge, mass, and anomalous magnetic moment of the nucleon. The second order terms in the photon energy describe the response of the nucleon's internal structure to an electric or magnetic dipole field. They are given by the following effective interaction :

$$H_{\text{eff}}^{(2)} = -4\pi \left[ \frac{1}{2} \alpha_{E1} \mathbf{E}^2 + \frac{1}{2} \beta_{M1} \mathbf{H}^2 \right], \quad (1)$$

where the proportionality coefficients are the electric ( $\alpha_{E1}$ ) and magnetic ( $\beta_{M1}$ ) scalar dipole polarizabilities, respectively. These global structure coefficients are proportional to the electric and magnetic dipole moments of the nucleon which are induced by the applied electric and magnetic fields. The polarizabilities have been measured extensively by use of unpolarized Compton scattering. A global fit to all modern low-energy proton Compton scattering data leads to the results [6]

$$\begin{aligned} \alpha_{E1}^p &= 12.1 \pm 0.3 \text{ (stat.)} \mp 0.4 \text{ (syst.)} \pm 0.3 \text{ (mod.)} , \\ \beta_{M1}^p &= 1.6 \pm 0.4 \text{ (stat.)} \pm 0.4 \text{ (syst.)} \pm 0.4 \text{ (mod.)} . \end{aligned} \quad (2)$$

Here and in the following the scalar polarizabilities are given in units of  $10^{-4} \text{ fm}^3$ , and the indicated errors denote the statistical, systematical and model-dependent errors. Equation 2 shows the dominance of the electric polarizability  $\alpha_{E1}^p$ . The tiny value of the magnetic polarizability,  $\beta_{M1}^p$ , originates from a strong cancelation between the large paramagnetic contribution of the  $N \rightarrow \Delta$  spin-flip transition and a nearly equally large diamagnetic contribution, mostly due to pion-loop effects.

The internal spin structure of the nucleon appears at third order in an expansion of the Compton scattering amplitude. It is described by the effective interaction

$$\begin{aligned} H_{\text{eff}}^{(3)} &= -4\pi \left[ \frac{1}{2} \gamma_{E1E1} \boldsymbol{\sigma} \cdot (\mathbf{E} \times \dot{\mathbf{E}}) + \frac{1}{2} \gamma_{M1M1} \boldsymbol{\sigma} \cdot (\mathbf{H} \times \dot{\mathbf{H}}) \right. \\ &\quad \left. - \gamma_{M1E2} E_{ij} \sigma_i H_j + \gamma_{E1M2} H_{ij} \sigma_i E_j \right], \end{aligned} \quad (3)$$

which involves one derivative of the fields with regard to either time or space,  $\dot{\mathbf{E}} = \partial_t \mathbf{E}$  and  $E_{ij} = \frac{1}{2}(\nabla_i E_j + \nabla_j E_i)$ , respectively. The four spin (or vector) polarizabilities  $\gamma_{E1E1}$ ,  $\gamma_{M1M1}$ ,  $\gamma_{M1E2}$ , and  $\gamma_{E1M2}$  describing the nucleon spin response at third order, can be related to a multipole expansion [7], as is reflected in the subscript notation. For example,  $\gamma_{M1E2}$  corresponds to the excitation of the nucleon by an electric quadrupole ( $E2$ ) field and its de-excitation by a magnetic dipole ( $M1$ ) field. Expanding the Compton scattering amplitude to higher orders in the energy, one obtains higher order polarizabilities to the respective order, e.g., the quadrupole polarizabilities at fourth order [7,8].

On the experimental side, much less is known about the spin polarizabilities, except for the forward ( $\gamma_0$ ) and backward ( $\gamma_\pi$ ) spin polarizabilities of the proton, given by the following linear combinations of the polarizabilities in Eq. (3):

$$\gamma_0 = -\gamma_{E1E1} - \gamma_{M1M1} - \gamma_{E1M2} - \gamma_{M1E2}, \quad (4)$$

$$\gamma_\pi = -\gamma_{E1E1} + \gamma_{M1M1} - \gamma_{E1M2} + \gamma_{M1E2}. \quad (5)$$

The forward spin polarizability has been determined by the Gerasimov-Drell-Hearn sum rule experiments at MAMI and ELSA [9,10,11]. A recent analysis of these data

yields the value [39]

$$\gamma_0 = -0.90 \pm 0.08 \text{ (stat.)} \pm 0.11 \text{ (syst.)} , \quad (6)$$

where here and in the following all spin polarizabilities are given in units of  $10^{-4} \text{ fm}^4$ . The recent experimental value for the backward spin polarizability has been obtained by a dispersive analysis of backward-angle Compton scattering [4],

$$\gamma_\pi = -38.7 \pm 1.8 \text{ (stat. + syst.)} . \quad (7)$$

This value includes both the dispersive and the large  $\pi^0$ -pole contributions. In the analysis of Ref. [4], the latter contribution takes the value  $\gamma_{\pi^0\text{-pole}} = -46.7$ , which leads to  $\gamma_\pi^{\text{disp}} = 8.0 \pm 1.8$ .

The effective Hamiltonians of Eqs. (1) and (3) describe a shift in the nucleon energies at second order in the electromagnetic (e.m.) fields. Several lattice QCD collaborations have recently implemented this fact as a tool to “measure” the nucleon polarizabilities by calculating the mass shifts in a constant background field and isolating the quadratic response. In particular, it has been possible to determine the electric polarizability of the neutron and other neutral octet and decuplet baryons [12] as well as the magnetic polarizability of the proton, the neutron, and all other particles in the lowest baryon octet and decuplet states [13]. In Ref. [13],  $\beta_{M1}^p$  has been calculated by use of the Wilson action in the pion mass range  $0.5 \leq m_\pi \leq 1 \text{ GeV}$  and neglecting disconnected loop diagrams. For the smallest calculated pion mass of  $m_\pi \simeq 500 \text{ MeV}$ , a value of  $\beta_{M1}^p = 2.36 \pm 1.20$  was obtained. While it is encouraging to see that the lattice result is in the right ballpark when compared to the experimental value of Eq. (2), a more precise comparison clearly requires a dynamical fermion calculation, including disconnected loop diagrams and much smaller pion masses. Such small pion masses would then allow one to extrapolate safely to the physical pion mass within the framework of chiral perturbation theory.

To determine the spin polarizabilities, Eq. (3) can likewise be used to calculate energy shifts of a polarized nucleon in an external field. As an example, consider a nucleon polarized along the  $z$ -axis and apply a magnetic field rotating with angular frequency  $\omega$  in the  $xy$  plane,

$$\mathbf{H} = B_0 [\cos(\omega t) \hat{e}_x + \sin(\omega t) \hat{e}_y] , \quad (8)$$

where  $\hat{e}_i$  stands for the unit vector in the direction  $i = x, y$  and  $B_0$  is the magnitude of the field. Such a field leads to an energy shift  $\Delta E = \mp 2\pi\gamma_{M1M1}\omega B_0^2$  if the nucleon spin is oriented along the positive (−) or negative (+)  $z$ -axis. The split between the two levels is then directly proportional to the magnetic dipole spin polarizability  $\gamma_{M1M1}$ . It has been shown in Ref. [14] that allowing for background fields with suitable variations in space and time, lattice QCD should be able to calculate all six dipole polarizabilities. In particular, calculations are in progress to determine the electric polarizability of a charged particle such as the proton as well as the four proton spin polarizabilities of Eq. (3) [15].

A microscopic understanding of the nucleon’s polarizabilities requires to quantify the interplay between resonance contributions, e.g., the  $N \rightarrow \Delta$  transition, and long range pion-cloud effects. Systematic studies of such pion-cloud effects became possible with the development of chiral perturbation theory (ChPT), by an expansion of the lagrangian in the external momenta and the pion mass (“ $p$ -expansion”). The first such calculation at leading order,  $\mathcal{O}(p^3)$ , yielded the following values for the proton scalar polarizabilities [16]:

$$\alpha_{E1}^p = 10\beta_{M1}^p = \frac{5\alpha_{em}g_A^2}{96\pi f_\pi^2 m_\pi} = 12.2 , \quad (9)$$

**Table 1.** Theoretical predictions for the dispersive contribution to spin polarizabilities of the proton: to  $\mathcal{O}(p^3)$  in HBChPT [17], to  $\mathcal{O}(p^4)$  in HBChPT [18], to  $\mathcal{O}(\varepsilon^3)$  in the small scale expansion [19], in the Lorentz covariant (LC) ChPT to  $\mathcal{O}(p^4)$  [21], in the chiral approach with unitarity and causality (GLP) of Ref. [20], in fixed- $t$  dispersion relations analysis (HDPV) of Ref. [8] and Ref. [7] (BGLMN), and in hyperbolic DRs of Ref. [1] (HYP. DRs).

	$\mathcal{O}(p^3)$	$\mathcal{O}(p^4)$	$\mathcal{O}(\varepsilon^3)$	LC	GLP	HDPV	BGLMN	HYP. DRs
$\gamma_{E1E1}$	-5.7	-1.4	-5.4	-2.8	-3.7	-4.3	-3.4	-3.8
$\gamma_{M1M1}$	-1.1	3.3	1.4	-3.1	2.5	2.9	2.7	2.9
$\gamma_{E1M2}$	1.1	0.2	1.0	0.8	1.2	-0.01	0.3	0.5
$\gamma_{M1E2}$	1.1	1.8	1.0	0.3	1.2	2.1	1.9	1.6
$\gamma_0$	4.6	-3.9	2.0	4.8	-1.2	-0.7	-1.5	-1.1
$\gamma_\pi$	4.6	6.3	6.8	-0.8	6.1	9.3	7.8	7.8

where  $\alpha_{em} = 1/137$ ,  $g_A \simeq 1.27$ , and  $f_\pi = 92.4$  MeV. This result is in remarkable agreement with the experimental result of Eq. (2). It also illustrates that these quantities diverge in the chiral limit, which is a challenge for the lattice QCD calculations. Conversely, the chiral expansion converges well in the “small  $m_\pi$ ” regime, and therefore ChPT can complement the lattice calculations by extrapolation to the physical pion mass. The ChPT work was extended to  $\mathcal{O}(p^4)$  within the heavy-baryon expansion [22], yielding  $\alpha_{E1}^p = 10.5 \pm 2.0$  and  $\beta_{M1}^p = 3.5 \pm 3.6$ . The error bars for these values indicate that several low-energy constants had to be determined by resonance saturation, e.g., by putting in phenomenological information about resonance and vector mesons. Since the  $\Delta(1232)$  lies close in energy, it has been proposed to include the resonance dynamically. This leads to an additional expansion parameter, the  $N\Delta$  mass splitting ( $\epsilon$  expansion). Unfortunately, at  $\mathcal{O}(\varepsilon^3)$  the “dynamical”  $\Delta$  increases the polarizabilities to values far above the data,  $\alpha_{E1}^p = 16.4$  and  $\beta_{M1}^p = 9.1$ . This can be changed by introducing large low-energy constants within a higher-order calculation, however, at expense of losing the predictive power [23]. More recently Pascalutsa and Phillips [24] proposed an alternative treatment in which the power counting changes between the threshold and the resonance regions, depending on which scales are enhanced. At low energies they introduce the ratio  $\delta$ , with  $\delta = (M_\Delta - M_N)/M_N$  as new expansion parameter. In this scheme, the values for the scalar polarizabilities at N<sup>3</sup>LO are  $\alpha_{E1}^p = 10.8 \pm 0.7$  and  $\beta_{M1}^p = 4.0 \pm 0.7$ , where the error bar is an estimate of higher-order contributions [25], and show a much improved agreement with experiment.

Results within different theoretical approaches for the dispersive contribution to the spin polarizabilities are collected in Table 1. The predictions from unsubtracted fixed- $t$  dispersion relations (DRs) are based on different inputs for the pion photoproduction amplitudes, while the results from hyperbolic DRs are obtained from dispersion integrals which run along a path at fixed angle. The agreement between the different DR results in Table 1 is quite satisfactory in all cases, and the spread among the predicted values can be seen as the best possible error estimate of such calculations to date. The ChPT predictions in the heavy baryon, small-scale expansion and Lorentz-covariant approach disagree in some cases, both among each other and with the DR results. In particular, issues about the convergence of the chiral expansion for the spin polarizabilities deserve further studies. In Table 1 we also quote the results from a recent approach based on the chiral Lagrangian at order  $\mathcal{O}(p^3)$  involving pion, nucleon and photon fields, and without isobar fields as explicit degrees of freedom (see column labeled “GLP”) [20]. The physics of the isobar resonances is included by infinite summation of higher order counter terms in the chiral Lagrangian, taking into account the constraints from unitarity and causality. In this framework, the au-

thors of Ref. [26] were able to give an unified description of photon- and pion-nucleon scattering data up to and beyond the isobar region, with the same set of parameters adjusted to pion-nucleon scattering data. For  $\gamma_{E_1 M_2}$  and  $\gamma_{M_1 E_2}$ , the ChPT results at  $\mathcal{O}(p^3)$  are recovered within small numerical deviations (compare columns  $\mathcal{O}(p^3)$  and GLP in Table 1), which are due to different values used for the parameters used in the calculations. In contrast, the ChPT and GLP results for  $\gamma_{E_1 E_1}$  and  $\gamma_{M_1 M_1}$  are at variance because of large rescattering effects, and the GLP values are in much better agreement with the predictions from DRs. The GLP scheme shows distinct indications of an improved convergence pattern as compared to ChPT, as was also observed for neutral-pion photoproduction [26]. However, these expectations for the spin polarizabilities need to be confirmed by explicit calculations.

### 3 Extraction of RCS polarizabilities

The extraction of polarizabilities from RCS data has been performed by three techniques. The first one is a low-energy expansion (LEX) of the Compton cross sections. Unfortunately this procedure is only applicable at photon energies well below 100 MeV, which makes a precise extraction a rather challenging task. The sensitivity to the polarizabilities is increased by measuring Compton scattering observables around pion threshold and into the  $\Delta(1232)$  resonance region. A second formalism which has been successfully applied to Compton data is based on DRs, in particular unsubtracted [27] and subtracted [28] fixed- $t$  DRs were used to extract the scalar polarizabilities of Eq. (2). A third approach has been developed within the framework of chiral effective field theories [23,24,25,29,30]. For energies below and around pion threshold the full Compton scattering process has been calculated to  $\mathcal{O}(p^4)$ , allowing for an independent extraction of the polarizabilities from Compton scattering data. The thus obtained values for  $\alpha_{E_1}^p$  and  $\beta_{M_1}^p$  in the work of [23,29] are nicely compatible with the results given by Eq. (2). Recently, the “ $\delta$ -counting” scheme has been applied to extract the scalar polarizabilities using a subset of low-energy data up to  $E_\gamma = 149$  MeV [25], and a preliminary study in a larger energy range has been presented in [31]. Both these analyses tend to favor a larger value for  $\beta_{M_1}^p$  than given by Eq. (2). These findings call for new dedicated measurements below pion threshold. In particular, it has been suggested that the sensitivity to the scalar polarizabilities can be enhanced by combination of unpolarized cross sections and data obtained with linearly polarized photons in particular kinematics. Proposals for such measurements below pion threshold have been presented at the HI $\gamma$ S facility at Duke [32].

Because a reliable data analysis is based on DRs, we recall some pertinent features of this technique in the following. The  $T$  matrix of RCS can be expressed by 6 independent structure functions  $A_i(\nu, t)$  [27]. These functions depend on the variables  $\nu$  and  $t$ , which are related to the initial ( $E_\gamma$ ) and final ( $E'_\gamma$ ) photon laboratory energies, and to the scattering angle  $\theta_{\text{lab}}$  by  $t = -4E_\gamma E'_\gamma \sin^2(\theta_{\text{lab}}/2)$  and  $\nu = E_\gamma + t/(4M_N)$ . The invariant amplitudes  $A_i$  are free of kinematical singularities and constraints, they also obey crossing symmetry and gauge invariance. Assuming further analyticity and an appropriate high-energy behavior, these amplitudes fulfill unsubtracted DRs at fixed  $t$ ,

$$\text{Re } A_i(\nu, t) = A_i^{\text{pole}}(\nu, t) + \frac{2}{\pi} \mathcal{P} \int_{\nu_0}^{\infty} d\nu' \frac{\nu' \text{Im } A_i(\nu', t)}{\nu'^2 - \nu^2}, \quad (10)$$

where  $A_i^{\text{pole}}$  is the nucleon pole term,  $\nu_0$  is the pion production threshold and  $\mathcal{P}$  denotes the principal value integral. The latter can be calculated if the absorptive part of the amplitude,  $\text{Im } A_i$ , is known to a sufficient accuracy. Because of the energy weighting, the pion production near threshold and the mesonic decay of the

low-lying resonances yield the biggest contributions to the integral. With the existing information on these processes and some reasonable assumptions on the lesser known higher part of the spectrum, the integrand can be constructed up to cm energies  $W \approx 2$  GeV. However, Regge theory predicts that the amplitudes  $A_1$  and  $A_2$  do not drop sufficiently fast to warrant a convergence of the integral. This behavior is mainly due to fixed poles in the  $t$  channel. In particular the  $t$ -channel exchange of pions and  $\sigma$  mesons leads to the bad convergence for  $A_2$  and  $A_1$ , respectively. The latter meson has a mass of about 600 MeV and a very large width, it models correlations in the two-pion channel with spin and isospin zero and positive parity. In order to obtain useful results for these two amplitudes, [27] proposed to close the contour integral in the complex plane by a semi-circle of finite radius  $\nu_{max}$ , and to replace the contribution from the semi-circle by a number of energy independent poles in the  $t$  channel. This procedure is relatively safe for  $A_2$  because the  $\pi^0$  pole or triangle anomaly is well established by both experiment and theory. However, it introduces a considerable model-dependence for  $A_1$ .

In order to avoid the convergence problem and the phenomenology necessary to determine the asymptotic contributions, it was suggested to subtract the DRs at  $\nu = 0$  [28]. This subtraction improves the convergence by two additional powers of  $\nu'$  in the denominator of the dispersion integrals, Eq. (10). The subtraction functions  $A_i(\nu = 0, t)$  can be obtained from subtracted DRs in  $t$  with the imaginary part of the amplitude  $\gamma\gamma \rightarrow \pi\pi \rightarrow N\bar{N}$  as input. In a first step, a unitarized amplitude for the  $\gamma\gamma \rightarrow \pi\pi$  subprocess is constructed from the available experimental data. This information is then combined with the  $\pi\pi \rightarrow N\bar{N}$  amplitudes determined by analytic continuation of  $\pi N$  scattering amplitudes [33]. Once the  $t$  dependence of the subtraction functions  $A_i(0, t)$  is known, the subtraction constants  $a_i = A_i(0, 0)$  have to be fixed. The 6 subtraction constants  $a_1$  to  $a_6$  are given by linear combinations of the scalar and spin polarizabilities and can be used to fit the RCS data. In the analysis of unpolarized cross sections it is sufficient to fit  $a_1$  and  $a_2$ , or equivalently  $(\alpha_{E1} - \beta_{M1})$  and  $\gamma_\pi$  to the data. The remaining 4 subtraction constants can be calculated through an unsubtracted dispersion integral.

In Fig. 1 we show the differential cross sections measured at several laboratories, as a function of the lab photon energy and at different scattering angles. The solid and dashed lines correspond to the results from unsubtracted and subtracted fixed- $t$  DRs, respectively, as obtained for fixed values of  $\alpha_{E1}$ ,  $\beta_{M1}$  and  $\gamma_\pi$ . Except for extreme backward scattering, both approaches lead to nearly identical results. A fit to the data within the unsubtracted DR formalism yields the values in Eq. (2) for the scalar polarizabilities, and compatible results, within error bars, are also obtained from subtracted DRs [1]. Because both formalisms provide an independent cross-check for the extraction of the polarizabilities, we can conclude that the present analysis of the low-energy data is well under control. We also note that very similar results for the cross sections below pion threshold were recently obtained within the unitary approach of Ref. [20].

Because the unpolarized cross section is mainly sensitive to the scalar polarizabilities and to the backward spin polarizability, double polarization experiments will be required to get information on the individual spin polarizabilities. First measurements of these observables have recently started at MAMI [34]. The proposal is to measure three different observables, *i*) the photon-beam asymmetry  $\Sigma_3$  with linearly polarized photons, *ii*) the beam-target asymmetry  $\Sigma_{2z}$  with circularly polarized photons and a longitudinally polarized target, and *iii*) the beam-target asymmetry  $\Sigma_{2x}$  with circularly polarized photons and a transversely polarized target. The simulated data points with the expected error bars for 100 hours running time are shown in Fig 2, in comparison with the predictions from subtracted DRs obtained for different values of  $\gamma_{E1E1}$  and  $\gamma_{M1M1}$  [35]. From a preliminary analysis in Ref. [34], the pro-

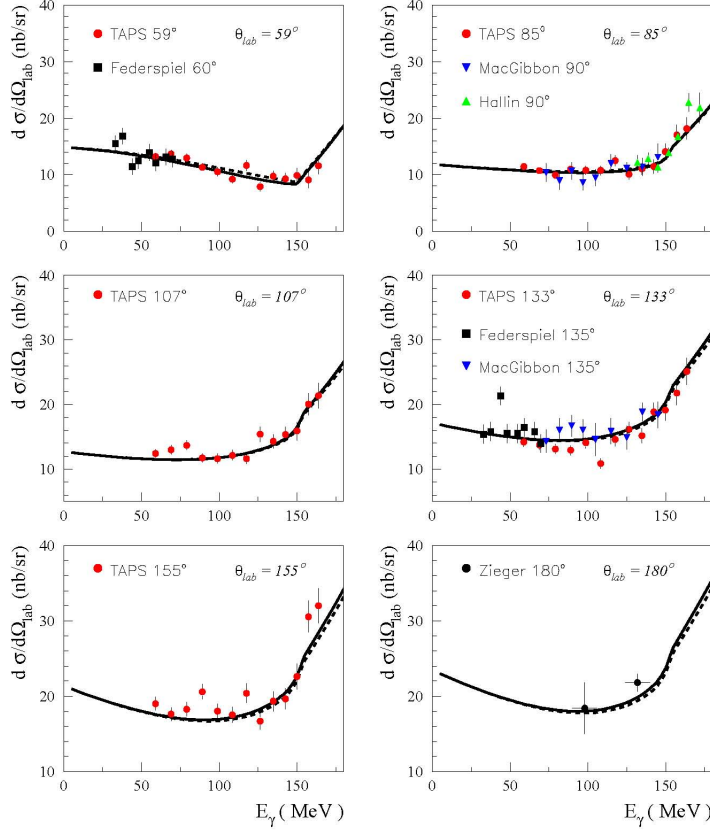


**Fig. 1.** Differential cross section for Compton scattering off the proton as a function of the lab photon energy  $E_\gamma$  and at different scattering angles. Solid lines: results from fixed- $t$  subtracted DRs, dashed lines: fixed- $t$  unsubtracted DRs. All results are shown for fixed values of  $\alpha_{E1} + \beta_{M1} = 13.8$ ,  $\alpha_{E1} - \beta_{M1} = 10$ , and  $\gamma_\pi = -37$ . The data are from Ref. [6] (full circles), Ref. [36] (diamonds), Ref. [37] (triangles), and Ref. [38] (open circles).

jected errors of the extracted spin polarizabilities are expected to be smaller than the spread of values presented in Table 1. Therefore, these experiments hold the promise to discriminate between the different theoretical predictions.

However, all the mentioned approaches for the extraction of the polarizabilities will necessarily contain some model dependence through parameters describing the high-energy regime. Such parameters are the low-energy constants appearing in ChPT, and in DRs the extrapolation of the photoproduction data to regions not covered by the experiment. Any additional confirmation of the theoretical framework by new alternative theoretical developments or independent experimental information is therefore most welcome.

To this aim, the DR calculation for the double polarization observables to be measured at MAMI, was recently compared with the unitary and causal approach based on the chiral Lagrangian of Refs. [20,26]. Although the two approaches are quite dif-

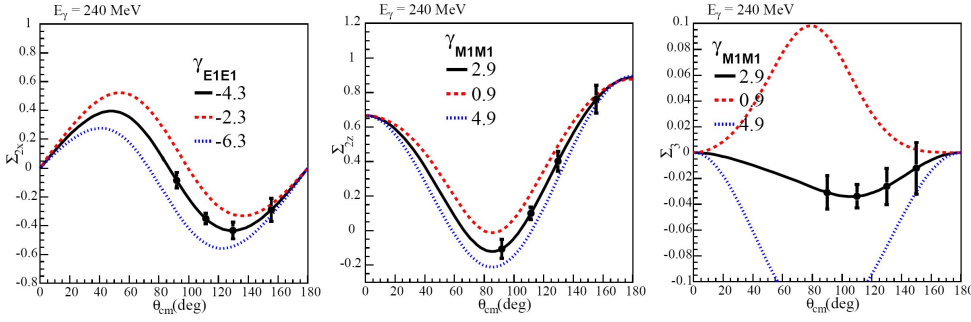


**Fig. 2.** The beam-target asymmetries  $\Sigma_{2x}$  (left),  $\Sigma_{2z}$  (center), and the beam asymmetry  $\Sigma_3$  (right), as function of the cm scattering angle at fixed photon energy  $E_\gamma = 240$  MeV. The different lines show the predictions of subtracted DRs using the experimental values for  $\alpha_{E1}$ ,  $\beta_{M1}$ ,  $\gamma_0$ , and  $\gamma_\pi$  as given by Eqs. (2), (6) and (7), while the remaining polarizabilities are free parameters. Left panel: results for fixed  $\gamma_{M1M1} = 2.9$  and values of  $\gamma_{E1E1}$  as indicated. Central and right panels: results for fixed  $\gamma_{E1E1} = -4.3$  and values of  $\gamma_{M1M1}$  as indicated. The plots are taken from the MAMI proposal [34], with the points representing simulated data with the expected error bars for 100 hours running time.

ferent in construction, they agree well below the pion-production threshold and start deviating slightly when the energy increases. The small difference between the two calculations at higher energies can be used to estimate the theoretical uncertainty in calculations of Compton scattering observables.

A second cross check was performed in Ref. [39], by comparing the “experimental” spin-dependent forward Compton scattering amplitude (as constructed from the available data on the helicity-dependent absorption cross sections) with the DR calculation obtained from different phenomenological inputs for the pion-photoproduction multipoles. The spin-dependent forward Compton scattering amplitude can be parametrized as

$$g(\nu) = -\frac{e^2 \kappa_N^2}{8\pi M_N^2} \nu + \gamma_0^{\text{dyn}}(\nu) \nu^3, \quad (11)$$

where the leading term is due to intermediate nucleon states (Born terms) and the higher-order contribution is described by the energy-dependent (dynamic) forward spin polarizability (FSP)  $\gamma_0^{\text{dyn}}(\nu)$ . This polarizability is a complex quantity which obeys the following DRs:

$$\text{Re}[\gamma_0^{\text{dyn}}(\nu)] = \frac{1}{4\pi^2} \mathcal{P} \int_{\nu_0}^{\infty} \frac{\sigma_{1/2}(\nu') - \sigma_{3/2}(\nu')}{\nu'(\nu'^2 - \nu^2)} d\nu', \quad (12)$$

$$\text{Im}[\gamma_0^{\text{dyn}}(\nu)] = \frac{\sigma_{1/2}(\nu) - \sigma_{3/2}(\nu)}{8\pi\nu^2}. \quad (13)$$

For  $\nu < \nu_0$  the imaginary part vanishes, and the dynamical FSP has a LEX with the leading-order contribution given by the forward polarizability  $\gamma_0$ . The “experimental” dynamical FSP is compared in Fig. 3 with the predictions based on different phenomenological parametrizations of the pion photoproduction multipoles [40,41,42,43]. The onset of  $S$ -wave pion production at  $E_\gamma = \nu_0$  leads to a strong cusp effect in the real part. The rapid increase of the dynamic FSP from its static value  $-0.90 \cdot 10^{-4} \text{ fm}^4$  at  $E_\gamma = 0$  to about  $6 \cdot 10^{-4} \text{ fm}^4$  at pion threshold clearly shows the necessity to analyze Compton scattering within the framework of dispersion analysis. In particular, such an approach is prerequisite in order to determine the 4 spin polarizabilities,



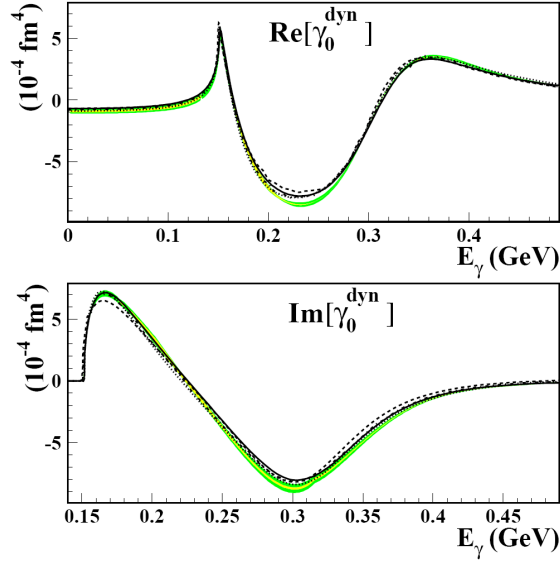


**Fig. 3.** The real (upper panel) and imaginary (lower panel) parts of the dynamic forward spin polarizability  $\gamma_0^{\text{dyn}}$  as function of the photon lab energy  $E_\gamma$ . The light grey (yellow) and dark grey (green) bands show the statistical and systematic uncertainties. The predictions are based on the pion photoproduction multipoles of Hanstein *et al.* [40] (solid line), SAID [41] (dotted line), MAID07 [42] (dashed line), and DMT [43] (dash-dotted line).

which yield significant contributions to the cross section only for photon energies above 80 MeV where the LEX does not apply. Except for the minimum of  $\text{Re}[\gamma_0^{\text{dyn}}]$  near  $E_\gamma = 0.23$  GeV, the experimental analysis is in very good agreement with the predictions of the presented models. The deviation in the minimum is not too surprising, because this comes about by a delicate balance between the positive contribution from the  $S$ -wave background and the negative contribution from the low-energy tail of the  $\Delta(1232)$  resonance.

#### 4 VCS and Generalized Polarizabilities

The VCS process on the proton is accessed through the  $ep \rightarrow ep\gamma$  reaction. In this process, the final photon can be emitted either by the proton, which is referred to as the fully virtual Compton scattering (FVCS) process, or by the lepton, which is referred to as the Bethe-Heitler (BH) process. The amplitude  $T^{ee'\gamma}$  of the  $ep \rightarrow ep\gamma$  reaction is given by the coherent sum of the BH and the FVCS process :  $T^{ee'\gamma} = T^{\text{BH}} + T^{\text{FVCS}}$ . The BH amplitude  $T^{\text{BH}}$  is exactly calculable from QED if one knows the nucleon e.m. form factors. The FVCS amplitude  $T^{\text{FVCS}}$  contains, in the one-photon exchange approximation, the VCS subprocess  $\gamma^*p \rightarrow \gamma p$ . The VCS amplitude can be further decomposed into a Born and a non-Born contribution. In the Born process, the virtual photon is absorbed on a nucleon and the intermediate state remains a nucleon, whereas the non-Born process contains all nucleon excitations and meson-loop contributions. The separation between Born and non-Born parts is performed as described in Ref. [44,45], to which we refer for the details. The behavior of the non-Born VCS contribution at low outgoing-photon energy  $E'_\gamma$  but at arbitrary three-momentum of the virtual photon, can be parametrized by 6 generalized polarizabilities

(GPs), which depend on the virtuality  $Q^2$  transferred by the virtual photon. The GPs are denoted by  $P^{(\mathcal{M}'L',\mathcal{M}L)S}(Q^2)$  [44,46,47]. In this notation,  $\mathcal{M}$  ( $\mathcal{M}'$ ) refers to the electric ( $E$ ), magnetic ( $M$ ) or longitudinal ( $L$ ) nature of the initial (final) photon,  $L$  ( $L'$ ) represents the angular momentum of the initial (final) photon, and  $S$  differentiates between the spin-flip ( $S = 1$ ) and non spin-flip ( $S = 0$ ) character of the transition at the nucleon side. Assuming that the emitted real photons have low energies, we may use the dipole approximation ( $L' = 1$ ). For a dipole transition in the final state, angular momentum and parity conservation lead to 10 GPs [44]. Furthermore, it has been shown [46] that nucleon crossing combined with charge conjugation symmetry of the VCS amplitudes provides 4 additional constraints among the 10 GPs, which leaves only 6 independent GPs.

In the limit of  $E'_\gamma \rightarrow 0$ , the VCS experiments can be analyzed in terms of LEXs, as proposed in Ref. [44]. These expansions are based on a low-energy theorem stating that the radiative amplitude for point-like particles diverges like  $1/E'_\gamma$  for  $E'_\gamma \rightarrow 0$ , whereas the dispersive amplitude vanishes like  $E'_\gamma$  in that limit. The interference between the  $1/E'_\gamma$  contribution of BH plus Born amplitudes and the leading term of the non-Born amplitude, can be expressed by 3 structure functions depending on the GPs,

$$\begin{aligned} P_{LL} &= -2\sqrt{6} M_N G_E P^{(L1,L1)0}, \\ P_{TT} &= -3G_M \frac{q^2}{\tilde{q}_0} \left( P^{(M1,M1)1} - \sqrt{2} \tilde{q}_0 P^{(L1,M2)1} \right), \\ P_{LT} &= \sqrt{\frac{3}{2}} \frac{M_N q}{Q} G_E P^{(M1,M1)0} + \frac{3}{2} \frac{Qq}{\tilde{q}_0} G_M P^{(L1,L1)1}, \end{aligned} \quad (14)$$

with  $G_E$  and  $G_M$  the electric and magnetic nucleon form factors. However, since the sensitivity of the VCS cross sections to the GPs grows with the photon energy, it is advantageous to go to higher photon energies, provided one can keep the theoretical uncertainties under control when approaching and crossing the pion threshold. The situation can be compared to RCS as described in Sec. 2, where it was shown that a DR formalism is prerequisite to extract the polarizabilities in the energy region above pion threshold where the observables are generally more sensitive to the GPs. In order to set up DRs for VCS, we describe the VCS tensor in terms of 12 independent amplitudes  $F_i$  ( $i = 1, \dots, 12$ ) which are free of kinematical singularities and constraints and even under crossing. These amplitudes depend on the 3 variables  $\nu$ ,  $t$  and  $Q^2$ , with  $\nu = E_\gamma + (t - Q^2)/(4M_N)$ , and  $t = 2E'_\gamma (\cos \theta_{\text{lab}} \sqrt{E_\gamma^2 + Q^2} - E_\gamma) - Q^2$ . Assuming further an appropriate analytic and high-energy behavior, these amplitudes fulfill unsubtracted DRs in the variable  $\nu$  and at fixed  $t$  and  $Q^2$ ,

$$\begin{aligned} \text{Re } F_i^{\text{nB}}(Q^2, \nu, t) &= F_i^{\text{pole}}(Q^2, \nu, t) - F_i^{\text{B}}(Q^2, \nu, t) \\ &+ \frac{2}{\pi} \mathcal{P} \int_{\nu_0}^{\infty} d\nu' \frac{\nu' \text{Im } F_i(Q^2, \nu', t)}{\nu'^2 - \nu^2}, \end{aligned} \quad (15)$$

where the pole amplitudes  $F_i^{\text{pole}}$  are obtained from the Born amplitudes at the pole position, that is, with all numerators evaluated at the pole. Furthermore,  $\text{Im } F_i$  are the discontinuities across the  $s$ -channel cuts, starting at the pion-production threshold, which can be calculated from the absorption cross sections due to  $\pi N$ ,  $\pi\pi N$ , and heavier hadronic states. As long as we are interested in the energy region up to the  $\Delta(1232)$ , we may saturate the  $s$ -channel dispersion integral by the  $\pi N$  contribution, choosing  $\nu_{\text{max}} \approx 1.5$  GeV as upper limit of integration and using empirical information from pion photo- and electroproduction as encoded in the MAID2007

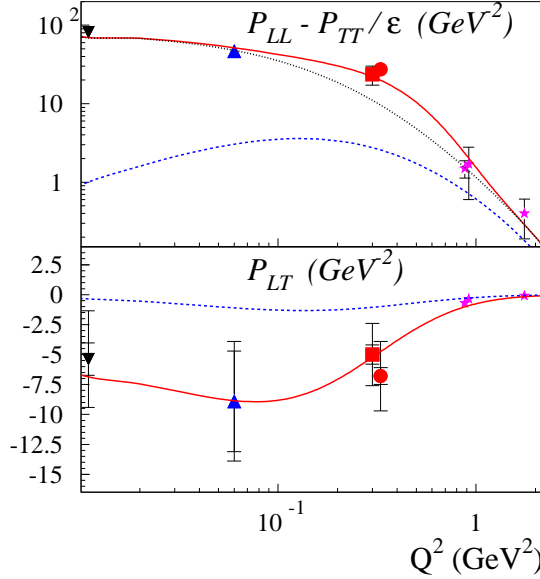


**Fig. 4.** The structure functions describing unpolarized VCS on a proton compared with the data from MAMI (circles [49], squares [50]), MIT-Bates (up triangles [51]), and JLab (stars [52]). The RCS data [6] are shown by the (black) down triangles (slightly displaced in  $Q^2$ ). All the lines are shown for  $\varepsilon = 0.645$  and based on the parameterizations of Eqs. (16) and (17) for the proton GPs. The lines in the upper panel correspond to different sets of parameters, dotted (black):  $\Lambda_\alpha = 0.7$  GeV,  $C_\alpha = 0$  (GP I), solid (red):  $\Lambda_\alpha = 0.7$  GeV,  $C_\alpha = -150$  GeV $^{-7}$  (GP II). The solid (red) line in the lower panel is obtained for  $\Lambda_\beta = 0.5$  GeV. The dashed (blue) lines in both panels show the contributions of the spin GPs.

parametrization [42]. However, Eq. (15) is only valid if the amplitudes drop fast enough such that the integrals converge. The high-energy behavior of the amplitudes  $F_i$  was investigated by [48] in the Regge limit ( $\nu \rightarrow \infty$ ,  $t$  and  $Q^2$  fixed), where it was found that the dispersion integrals diverge for two amplitudes,  $F_1$  and  $F_5$ . The asymptotic contributions to these amplitudes are described by the  $t$ -channel exchange of  $\sigma$  and  $\pi^0$  mesons, respectively, and other effects such as many-pion and heavier intermediate states in the  $s$ -channel integral. All these effects beyond the dispersive  $\pi N$  contribution are parametrized in terms of asymptotic contributions. In particular, the asymptotic part of the magnetic GP is described by a dipole function

$$P_{asy}^{(M1,M1)0}(Q^2) = P_{asy}^{(M1,M1)0}(0)/(1 + Q^2/\Lambda_\beta^2)^2. \quad (16)$$

To describe the electric GP, we allow for an asymptotic part consisting of a sum of a dipole and a Gaussian, in the same vein as the parametrization proposed in [53] for the nucleon form factors,

$$P_{asy}^{(L1,L1)0}(Q^2) = P_{asy}^{(L1,L1)0}(0)/(1 + Q^2/\Lambda_\alpha^2)^2 + C_\alpha Q^4 e^{-(Q^2-0.15)/0.15}. \quad (17)$$

The values at the real-photon point are fixed by the difference between the dispersive  $\pi N$  contribution and the empirical information for the proton electric and magnetic polarizabilities as obtained from RCS experiments [6], which leads to  $P_{asy}^{(L1,L1)0}(0) =$

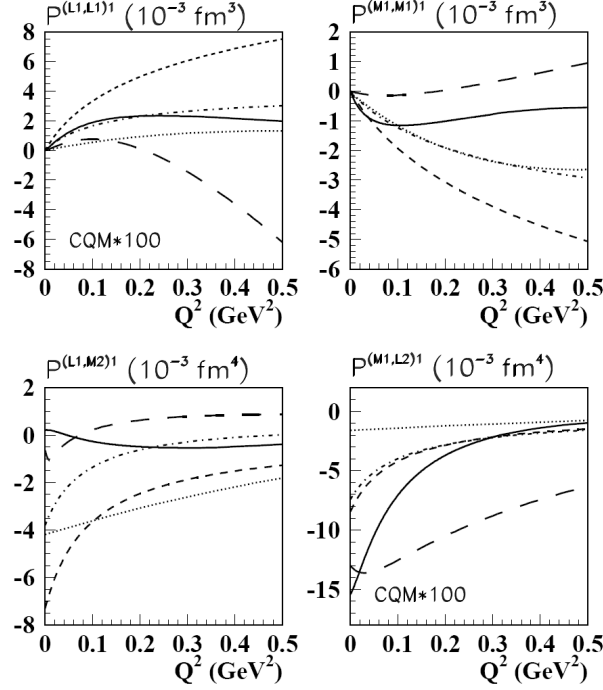


**Fig. 5.** The spin-flip GPs without the  $\pi^0$ -pole contribution. The lines shown correspond to the predictions from several calculations. Solid: dispersive  $\pi N$  contribution [48], short-dashed:  $\mathcal{O}(p^3)$  HBChPT [54,55], long-dashed:  $\mathcal{O}(p^4)$  HBChPT [56,57], dashed-dotted: linear  $\sigma$  model [58], dotted: non-relativistic CQM [59]. For visibility, the tiny CQM results for  $P^{(L1,L1)1}$  and  $P^{(M1,L2)1}$  are multiplied by a factor 100.

$-14.37 \text{ GeV}^{-3}$ , and  $P_{asy}^{(M1,M1)0}(0) = 21.82 \text{ GeV}^{-3}$ . The remaining three parameters  $A_\beta$ ,  $A_\alpha$ , and  $C_\alpha$  describe the  $Q^2$  dependence of the asymptotic parts of the spin-independent GPs and can be determined by a fit to the available VCS data. In the upper panel of Fig. 4, we show the comparison with the experimentally measured unpolarized structure functions  $P_{LL} - P_{TT}/\varepsilon$  ( $P_{LT}$ ), which is proportional to the electric (magnetic) GPs respectively, up to a small spin-GP contribution (dashed lines). The magnetic GP is essentially given by  $P_{LT}$  shown in the lower panel of Fig. 4. The figure shows that all the data can be well described by  $A_\beta = 0.5 \text{ GeV}$ . For the electric GP, a fit to the MIT-Bates and JLab data is obtained for  $C_\alpha = 0$ , and  $A_\alpha = 0.7 \text{ GeV}$  (denoted by parameterization GP I). However, this does not describe the MAMI data at intermediate  $Q^2$ , which require an additional structure, parameterized through the Gaussian term in Eq. (17). A good description of all available data is obtained for  $A_\alpha = 0.7 \text{ GeV}$ , and  $C_\alpha = -150 \text{ GeV}^{-7}$  (denoted by parameterization GP II).

The GPs were also calculated in HBChPT at  $\mathcal{O}(p^3)$  [54,55] and at  $\mathcal{O}(p^4)$  [56,57]. Although the HBChPT and DR results agree qualitatively in the description of the unpolarized VCS structure functions, there are large differences in the spin sector. Figure 5 shows the predictions for the spin GPs for several different approaches. The comparison demonstrates that a satisfying theoretical description of the spin-flip GPs over a large range in  $Q^2$  is still a challenging task. This calls for VCS experiments which are sensitive to the spin GPs. Two types of such experiments can be envisaged: (i) unpo-

larized VCS with variation of the transverse photon polarization  $\epsilon$  in order to separate the response functions  $P_{LL}$  and  $P_{TT}$  and (ii) double-polarization experiments to access new structure functions directly related to the spin-flip GPs [60]. A first test experiment for double-polarization observables was performed at MAMI [61]. Furthermore, these structure coefficients are also prominent input in calculating hadronic corrections to the Lamb shift [62] and the hyperfine splitting in hydrogen [63].

## 5 Spatial representation of GPs

In the last years, generalized parton distributions [64,65] and form factors [66,67] have been discussed as a tool to access the distributions of partons in the transverse plane, and first calculations of these spatial distributions have been performed in lattice QCD [68] and hadronic models [69]. Most recently, it has also been shown how the concept of GPs can be used to describe the spatial deformation of the charge and magnetization densities if the nucleon is exposed to an external quasi-static electric field [70,71].

In order to arrive at a spatial representation of the information contained in the GPs, we consider the VCS process in a light-front frame [71]. The VCS tensor is defined as

$$H^{\mu\nu} = -i \int d^4x e^{-iq \cdot x} \langle p', \lambda'_N | T [J^\mu(x), J^\nu(0)] | p, \lambda_N \rangle, \quad (18)$$

with  $\lambda_N$  and  $p$  ( $\lambda'_N$  and  $p'$ ) the helicity and four-momentum of the initial (final) nucleon. We indicate the (large) light-front  $+$  component by  $P^+ = (p^+ + p'^+)/2$  (defining  $a^\pm \equiv a^0 \pm a^3$ ), and choose the symmetric frame by requiring that  $\Delta = p' - p$  is purely transversal, i.e.  $\Delta^+ = 0$ . In the light-front frame, the  $+$  component of the current  $J^\mu$  in (18) is a positive-definite operator for each quark flavor, allowing for a light-front charge density interpretation. In the low-energy limit  $\nu \rightarrow 0$ , the VCS light-front helicity amplitude  $H(\lambda'_\gamma, \lambda'_N, \lambda_N) \equiv \varepsilon_\nu'^*(\lambda'_\gamma) H^{+\nu}$  can be described in terms of GPs. In particular, we consider the transverse polarization component of the outgoing photon corresponding to an electric field  $\mathbf{E} \sim i E'_\gamma \epsilon'_\perp$ . Any system of charges will respond to such an applied electric field through an induced polarization  $\mathbf{P}_0$ , which will be forced to align with the external field such as to minimize the energy  $-\mathbf{E} \cdot \mathbf{P}_0$ . The linear response in the outgoing-photon energy of the helicity averaged VCS amplitude therefore allows one to define an induced polarization  $\mathbf{P}_0$  as

$$\varepsilon_\perp'^*(\lambda'_\gamma) \cdot \mathbf{P}_0 \equiv \frac{(1 + \tau)}{(2P^+)} \frac{\partial}{\partial \nu} H(\lambda'_\gamma, \lambda_N, \lambda_N) \big|_{\nu=0}, \quad (19)$$

where  $\tau \equiv Q^2/(4M_N^2)$ . By Fourier transforming  $\mathbf{P}_0$ , we obtain the spatial distortion of the charge density in an unpolarized nucleon as induced by the external electric field,

$$\mathbf{P}_0(\mathbf{b}) = \hat{b} \int_0^\infty \frac{dQ}{(2\pi)} Q J_1(bQ) A(Q^2), \quad (20)$$

where  $\mathbf{b}$  is the transverse position,  $b = |\mathbf{b}|$ , and  $\hat{b} = \mathbf{b}/b$  and  $A(Q^2)$  can be expressed in terms of the scalar and spin GPs. The dipole pattern described by Eq. (20) is shown in Fig. 6 for the parameterizations GP I and GP II in the left and right panels, respectively. The comparison shows that the enhancement at intermediate  $Q^2$  in GP II (second term in Eq. (17)) gives rise to a much larger transverse extension of the induced polarization cloud. Forthcoming VCS experiments planned at MAMI [72] are conceived to study the  $Q^2$  dependence of the GPs in more detail. In this way, the experiment is expected to verify or disprove the large distance structure predicted by

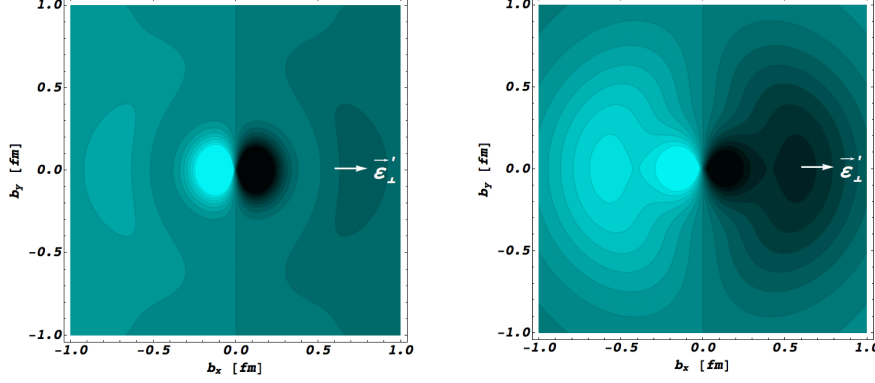


**Fig. 6.** The induced polarization  $P_0^x$  in a proton of definite light-cone helicity if exposed to an e.m. field with photon polarization along the  $x$ -axis, as indicated. The left (right) panel is obtained for GP I (GP II), see caption of Fig. 4. The light (dark) regions correspond to the largest (smallest) values.

model GP II.

Analogously, we can define the linear response to an external quasi-static e.m. dipole field if the nucleon is in an eigenstate of transverse spin,  $\mathbf{S}_\perp \equiv \cos \phi_S \hat{e}_x + \sin \phi_S \hat{e}_y$ , with  $\phi_S$  the angle indicating the spin vector direction. The dependence of the induced polarization  $\mathbf{P}_T$  on the transverse position is given by

$$\begin{aligned} \mathbf{P}_T(\mathbf{b}) = & \mathbf{P}_0(\mathbf{b}) - \hat{b} (\mathbf{S}_\perp \times \mathbf{e}_z) \cdot \hat{b} \int_0^\infty \frac{dQ}{(2\pi)} Q J_2(bQ) B \\ & + (\mathbf{S}_\perp \times \mathbf{e}_z) \int_0^\infty \frac{dQ}{(2\pi)} Q \left[ J_0(bQ) C + \frac{J_1(bQ)}{bQ} B \right], \end{aligned} \quad (21)$$

displaying dipole, quadrupole and monopole patterns with weights  $B$ , and  $C$  given by combinations of scalar and spin GPs.

In Fig. 7 we show the spatial distributions in the induced polarization for a proton of transverse spin (chosen along the  $x$ -axis) for parameterization GP II. The component  $P_T^x - P_0^x$  displays a quadrupole pattern with pronounced strength around 0.5 fm due to the electric GP, whereas the component  $P_T^y - P_0^y$  shows an additional monopole pattern, which is dominated by the  $\pi^0$ -pole contribution.

## 6 Conclusions

In this contribution we have discussed real and virtual Compton scattering off the proton as powerful tools to extract information on the proton polarizabilities. In the case of RCS, the static scalar polarizabilities are now known with relatively small error bars, whereas our knowledge on the spin-dependent sector is as yet incomplete. Only two combinations of the spin polarizabilities have been determined as yet. However,

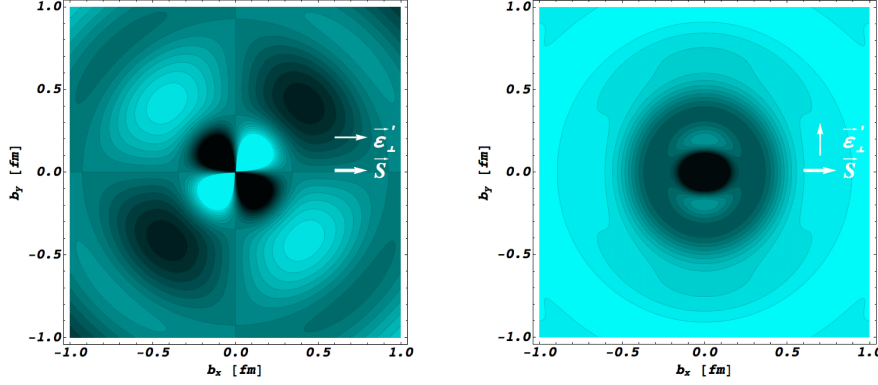


**Fig. 7.** The induced polarization density in a proton, with spin  $\mathbf{S}$  oriented along the  $x$ -axis, when submitted to an e.m. field. The left (right) panels are for  $P_T^x - P_0^x$  ( $P_T^y - P_0^y$ ), and correspond with photon polarization along the  $x$ -axis ( $y$ -axis) as indicated. The light (dark) regions correspond to the largest (smallest) values using parameterization GP II, see caption of Fig. 4.

the forthcoming double-polarization experiments at MAMI will allow us to disentangle all 6 spin-polarizabilities individually. The spin polarizabilities of the nucleon are fundamental structure constants of the nucleon, just as shape and size of this strongly interacting many-body system. Therefore, the ongoing experimental programs are both timely and important for our understanding of the nucleon structure. These activities will provide stringent precision tests for both the existing predictions of effective field theories and future results expected from the lattice-gauge community for the polarizability of the nucleon.

Moreover, the generalized polarizabilities from VCS processes allow us to map out the spatial dependence of the induced polarizations in an external e.m. field. The existing field theoretical formalism to extract light-front densities from nucleon form factor data has been recently extended to the deformations of quark charge densities under the influence of an applied e.m. field. It has been shown that the available proton electric GP data yield a pronounced structure in the induced polarization density at large transverse distances of  $0.5 - 1$  fm. At  $Q^2$  values smaller than  $0.1 \text{ GeV}^2$ , chiral effective field theory was found to describe the VCS data quite well, which highlights the role of pions in the nucleon structure. Such description can however not be applied at intermediate and large  $Q^2$  values. This transition region is dominated by nucleon resonance structure, which can be described by dispersion relations. Forthcoming VCS precision experiments at MAMI in this intermediate  $Q^2$  region will be capable to determine the spin polarizabilities in more detail and, in this way, help to unravel the distribution of quark charge and magnetization currents in the nucleon.

The authors are grateful to all the collaborators with whom many of the presented results were obtained. We also acknowledge the support by the Collaborative Research Center 443 (SFB 443) of the Deutsche Forschungsgemeinschaft.

## References

1. D. Drechsel, B. Pasquini and M. Vanderhaeghen, Phys. Rept. **378**, (2003) 99.
2. D. Drechsel and T. Walcher, Rev. Mod. Phys. **80**, (2008) 731.
3. P. A. M. Guichon and M. Vanderhaeghen, Prog. Part. Nucl. Phys. **41**, (1998) 125.
4. M. Schumacher, Prog. Part. Nucl. Phys. **55**, (2005) 567.
5. H. Fonvieille, these proceedings.
6. V. Olmos de Leon *et al.*, Eur. Phys. J. A **10**, (2001) 207.
7. D. Babusci, G. Giordano, A. I. L'vov, G. Matone and A. M. Nathan, Phys. Rev. C **58**, (1998) 1013.
8. B. R. Holstein, D. Drechsel, B. Pasquini and M. Vanderhaeghen, Phys. Rev. C **61**, (2000) 034316.
9. J. Ahrens *et al.* [GDH Coll. and A2 Coll.], Phys. Rev. Lett. **87**, (2001) 022003.
10. H. Dutz *et al.* [GDH Coll.], Phys. Rev. Lett. **91**, (2003) 192001.
11. H. Dutz *et al.* [GDH Coll.], Phys. Rev. Lett. **93**, (2004) 032003.
12. J. Christensen, W. Wilcox, F. X. Lee, and L. M. Zhou, Phys. Rev. D **72**, (2005) 034503.
13. F. X. Lee, L. Zhou, W. Wilcox, and J. Christensen, Phys. Rev. D **73**, (2006) 034503.
14. W. Detmold, B. C. Tiburzi, and A. Walker-Loud, Phys. Rev. D **73**, (2006) 114505.
15. W. Detmold, A. Walker-Loud, and B. C. Tiburzi, arXiv:hep-lat/0610018.
16. V. Bernard, N. Kaiser and U. G. Meissner, Phys. Rev. Lett. **67**, (1991) 1515.
17. T. R. Hemmert, B. R. Holstein, J. Kambor and G. Knochlein, Phys. Rev. D **57**, (1998) 5746.
18. K. B. Vijaya Kumar, J. A. McGovern and M. C. Birse, Phys. Lett. B **479**, (2000) 167.
19. G. C. Gellas, T. R. Hemmert and U. G. Meissner, Phys. Rev. Lett. **86**, (2001) 3205.
20. A. M. Gasparyan, M. F. M. Lutz and B. Pasquini, arXiv:1102.3375 [hep-ph].
21. D. Djukanovic, Ph. D. dissertation, University of Mainz, (2008).
22. V. Bernard, N. Kaiser, A. Schmidt and U. G. Meissner, Phys. Lett. B **319**, (1993) 269; Z. Phys. A **348**, (1994) 317.
23. R. P. Hildebrandt, H. W. Griesshammer, T. R. Hemmert and B. Pasquini, Eur. Phys. J. A **20**, (2004) 293.
24. V. Pascalutsa and D. R. Phillips, Phys. Rev. C **67**, (2003) 055202.
25. V. Lensky and V. Pascalutsa, Eur. Phys. J. C **65**, (2010) 195; Pisma Zh. Eksp. Teor. Fiz. **89**, (2009) 127 [JETP Lett. **89**, (2009) 108].
26. A. Gasparyan and M. F. M. Lutz, Nucl. Phys. A **848**, (2010) 126.
27. A. I. L'vov, V. A. Petrun'kin and M. Schumacher, Phys. Rev. C **55**, (1997) 359.
28. D. Drechsel, M. Gorchtein, B. Pasquini and M. Vanderhaeghen, Phys. Rev. C **61**, (1999) 015204.
29. S. R. Beane, M. Malheiro, J. A. McGovern, D. R. Phillips and U. van Kolck, Nucl. Phys. A **747**, (2005) 311; Phys. Lett. B **567**, (2003) 200 [Erratum-ibid. B **607**, (2005) 320].
30. R. P. Hildebrandt, H. W. Griesshammer and T. R. Hemmert, Eur. Phys. J. A **20**, (2004) 329.
31. J. A. McGovern, H. W. Griesshammer, D. R. Phillips and D. Shukla, PoS **CD09**, (2009) 059.
32. H. R. Weller, *et al.*, Prog. Part. Nucl. Phys. **62**, (2009) 257.
33. G. Höhler, *Pion-Nucleon Scattering*, ed. H. Schopper, Landoldt-Boernstein (Springer, Berlin), I/9b2.
34. MAMI Proposal A2/11-2009, spokesperson: A. Thomas.
35. B. Pasquini, D. Drechsel and M. Vanderhaeghen, Phys. Rev. C **76**, (2007) 015203.
36. F. J. Federspiel *et al.*, Phys. Rev. Lett. **67**, (1991) 1511.
37. B. E. MacGibbon, *et al.*, Phys. Rev. C **52**, (1995) 2097.
38. A. Zieger, *et al.*, Phys. Lett. B **278**, (1992) 34.



39. B. Pasquini, P. Pedroni and D. Drechsel, Phys. Lett. B **687**, (2010) 160.
40. O. Hanstein, D. Drechsel, and L. Tiator, Nucl. Phys. A **632**, (1998) 561.
41. R. A. Arndt, W. J. Briscoe, I. I. Strakovsky, and R. L. Workman, Phys. Rev. C **66**, (2002) 055213.
42. D. Drechsel, S. S. Kamalov, and L. Tiator, Eur. Phys. J. A **34**, (2007) 69.
43. S.S. Kamalov, S.N. Yang, D. Drechsel, and L. Tiator Phys. Rev. C **64**, (2001) 032201.
44. P. A. M. Guichon, G. Q. Liu and A. W. Thomas, Nucl. Phys. A **591**, (1995) 606.
45. S. Scherer, A. Y. Korchin and J. H. Koch, Phys. Rev. C **54**, (1996) 904.
46. D. Drechsel, G. Knochlein, A. Y. Korchin, A. Metz and S. Scherer, Phys. Rev. C **57**, (1998) 941; *ibid* **58**, (1998) 1751.
47. D. Drechsel, G. Knochlein, A. Metz and S. Scherer, Phys. Rev. C **55**, (1997) 424.
48. B. Pasquini, D. Drechsel, M. Gorchtein, A. Metz and M. Vanderhaeghen, Phys. Rev. C **62**, (2000) 052201; Eur. Phys. J. A **11**, (2001) 185.
49. J. Roche *et al.* [VCS Coll. and A1 Coll.], Phys. Rev. Lett. **85**, (2000) 708.
50. P. Janssens *et al.* [A1 Coll.], Eur. Phys. J. A **37**, (2008) 1.
51. P. Bourgeois *et al.*, Phys. Rev. Lett. **97**, (2006) 212001.
52. G. Laveissiere *et al.* [Jefferson Lab Hall A Coll.], Phys. Rev. Lett. **93**, (2004) 122001.
53. J. Friedrich and T. Walcher, Eur. Phys. J. A **17**, (2003) 607.
54. T. R. Hemmert, B. R. Holstein, G. Knöchlein, S. Scherer, Phys. Rev. D **55**, (2000) 2630.
55. T. R. Hemmert, B. R. Holstein, G. Knochlein and D. Drechsel, Phys. Rev. D **62**, (2000) 014013.
56. C. W. Kao and M. Vanderhaeghen, Phys. Rev. Lett. **89**, (2002) 272002.
57. C. W. Kao, B. Pasquini and M. Vanderhaeghen, Phys. Rev. D **70**, (2004) 114004.
58. A. Metz and D. Drechsel, Z. Phys. A **356**, (1996) 351; Z. Phys. A **359**, (1997) 165.
59. B. Pasquini, S. Scherer and D. Drechsel, Phys. Rev. C **63**, (2001) 025205.
60. M. Vanderhaeghen, Phys. Lett. B **402**, (1997) 243.
61. MAMI Proposal A1/01-00, spokesperson: R. Neuhausen.
62. C. E. Carlson and M. Vanderhaeghen, arXiv:1101.5965 [hep-ph].
63. V. Nazaryan, C. E. Carlson and K. A. Griffioen, Phys. Rev. Lett. **96** (2006) 163001.
64. M. Burkardt, Phys. Rev. D **62**, (2000) 071503 [Erratum-*ibid.* D **66**, (2002) 119903]; Int. J. Mod. Phys. A **18**, (2003) 173.
65. M. Diehl and Ph. Hagler, Eur. Phys. J. C **44**, (2005) 87.
66. G. A. Miller, Phys. Rev. Lett. **99**, (2007) 112001.
67. C. E. Carlson and M. Vanderhaeghen, Phys. Rev. Lett. **100**, (2008) 032004.
68. LHPC Coll. and SESAM Coll., Phys. Rev. Lett. **93**, (2004) 112001.
69. B. Pasquini and S. Boffi, Phys. Lett. B **653**, (2007) 23.
70. A. I. L'vov, S. Scherer, B. Pasquini, C. Unkmeir and D. Drechsel, Phys. Rev. C **64**, (2001) 015203.
71. M. Gorchtein, C. Lorcé, B. Pasquini and M. Vanderhaeghen, Phys. Rev. Lett. **104**, (2010) 112001.
72. MAMI Proposal A1/1-2009, spokesperson: H. Merkel.